J Vis (2022) 25:1035–1046
https://doi.org/10.1007/s12650-022-00832-z

REGULAR PAPER

Ignazio Maria Viola · Alex Nila · Thomas Davey · Roman Gabl

Underwater LED-based Lagrangian particle tracking velocimetry

Received: 14 May 2021 / Revised: 25 January 2022 / Accepted: 13 February 2022 / Published online: 11 March 2022

Abstract A new white-light volumetric flow measurement technique is presented that can be used in large-scale facilities. The technique enables large volumes to be measured with high temporal and spatial resolution and without the need for a class-4 laser. This LED-based Lagrangian particle tracking velocimetry is demonstrated by measuring the tip vortex formation and the near wake of a 1.2 m diameter tidal turbine in a 25 m diameter, 2 m deep tank. Seven streamwise-distributed volumes of interest are combined, each 334 mm long, 244 mm wide and 140 mm deep, reaching up to one diameter downstream of the turbine. The system does not require re-calibration when moved. By assuming a periodic flow field, a phase-averaged flow field was reconstructed with a temporal resolution of 3.9 ms and a spatial resolution of 5.4 mm. The large volume and high time and spatial resolution could enable key research questions to be addressed on high-Reynolds-number flows and could provide valuable benchmark data for numerical model development and code validation.

Keywords Lagrangian particle tracking · Shake-The-Box · Flow diagnostics · LED illumination · Tidal turbine hydrodynamics · Tip vortex · Rotor wake

1 Introduction

Large marine facilities such as water tunnels, towing tanks and wave basins, are not always compatible with laser-based flow diagnostics techniques (Adrian et al. 2011; Raffel et al. 2018). Space- and time-resolved flow measurement capable of resolving the dynamics of key flow features typically requires Class 4 laser illumination (Fontaine et al. 2014; Lust et al. 2015; Shi et al. 2017; Nuernberg and Tao 2018; Gaurier et al. 2020). Class 4 lasers are highly dangerous because they can damage the eye and the skin causing blindness and burns, and they can cause fires. To ensure safe use of these lasers, the light is typically enclosed preventing accidental exposure through a physical barrier and other access safety controls (e.g. door interlocks) which are not practical in large scale facilities. In this paper, a first of its kind experimental apparatus is demonstrated that allows accurate flow visualization to be undertaken with only harmless white light illumination.

Only in recent years, eye-safe Light-Emitting Diode (LED) illumination has become sufficiently powerful to enable large-scale flow measurements through either Particle Image Velocimetry (PIV) or Lagrangian Particle Tracking Velocimetry (LPTV). The first applications of LED were in micro-PIV

I. M. Viola (✉) · T. Davey · R. Gabl
School of Engineering, Institute for Energy Systems, University of Edinburgh, Edinburgh EH9 3BF, UK
E-mail: i.m.viola@ed.ac.uk

A. Nila
LaVisionUK Ltd., Bicester OX26 6QB, UK

because of the low power requirements (Chételat and Kim 2002). In the last 10 years, LEDs have commonly been used for centimetre-scale field of views (Willert et al. 2010). In contrast, meter-scale time-resolved flow measurements have only recently become possible with LED illumination (Schanz et al. 2018).

This alternative light source has proven initially to be very attractive for large-scale air flow measurements such as those around live birds, for which laser illumination is a hazard (Usherwood et al. 2020). Whilst initially used with conventional multi-camera, large aperture imaging systems, LED illumination has more recently been used with a compact image system: the MiniShaker Coaxial Volumetric Velocimeter (CVV) produced by LaVision (Mertens et al. 2021). This velocimeter was originally used by Schneiders et al. (2018) with laser illumination. A key benefit of the MiniShaker is that it allows the image system to be moved without the need for re-calibration, and thus it is effective for measuring multiple volumes (Jux et al. 2018). These measurements can be stitched together in a post-processing phase to reconstruct time-averaged (or phase-averaged) results over an enlarged measurement volume.

The LPTV 'Shake-The-Box' (Schanz et al. 2016) is particularly suited for the computation of large volume flow fields of several litres, such as the above-mentioned studies (Schanz et al. 2018; Schneiders et al. 2018; Jux et al. 2018; Usherwood et al. 2020; Mertens et al. 2021). It enables measurements over large volumes and with a similar high particle image density as tomographic-PIV (Schanz et al. 2016).

Underwater volumetric measurements of several litres have only become feasible in recent years. For example, Roettig et al. (2019) used an underwater volumetric flow measurement with fibre-delivered laser illumination. In the same work, the authors also presented the potential of LED-based illumination for one of the test cases with promising results. However, to the best of the authors' knowledge, no in-depth work has been published using LED-based illumination underwater for volumetric full-field flow measurements.

Hence, in this paper, the first detailed application of LED illumination for large-scale flow measurements in water is presented. This is achieved with a LaVision MiniShaker, which is an integrated volumetric velocimeter akin to that used by Schneiders et al. (2018), but the illumination is not laser-based nor co-axial, but externally provided by LEDs. By translating rigidly the LEDs and the MiniShaker, seven adjacent volumes of 6 l each are measured. The images are processed with the 'Shake-The-Box' (STB) approach to compute the time-resolved flow fields of each volume, and the phase-locked flow field of the combined volume.

As an example application, we consider the near wake of a tidal turbine. The characterisation of tidal turbine wakes remains very challenging both experimentally and numerically (Day et al. 2015; Adcock et al. 2021). Due to the anisotropy of the wake and its wide range of temporal scales, experimental measurements are needed to inform numerical simulations on appropriate models (Afgan et al. 2013; Tedds et al. 2014; Lloyd et al. 2014; Olczak et al. 2016; Ahmed et al. 2017; Ouro and Stoesser 2019). The anisotropy of the wake turbulence does not only derive from the tip vortices and the global flow rotation around the turbine axis (Chamorro et al. 2013; Chen et al. 2017), but also because of the seabed and free-surface blockage that accelerates the bypass flow on the sides of the turbines (Tedds et al. 2014; Stallard et al. 2013, 2015; Chen et al. 2017). Here, a white-light LPTV is demonstrated to show how it can contribute to tackling some of these outstanding research questions.

This paper is organised as follows. In Sect. 2 (Experimental Conditions) the facility (Sect. 2.1) and the turbine (Sect. 2.2) used for this demonstration are presented. The flow conditions measured in the absence of the turbine are presented in Sect. 2.3. In Sect. 3 (Lagrangian Particle Tracking Velocimetry), the new system is presented in detail, including the hardware (Sect. 3.1), the calibration (Sect. 3.2) and the general data processing associated with the technique (Sect. 3.3). Section 4 (Example of Application) provides results and the associated specific data processing. This section is broken down into the visualisation of the formation of the tip vortices (Sect. 4.1) and of the overall flow in the near wake (Sect. 4.2). A discussion on the main results is included in Sect. 5 (Discussion and Conclusions).

2 Experimental condition

2.1 Facility

Tests are conducted in the FloWave Ocean Energy Research Facility of the University of Edinburgh, Scotland (Fig. 1). FloWave is a 25 m diameter and 2 m deep tank for testing offshore wave and current energy technologies in combined wave and current conditions. An array of 168 wave paddles along the perimeter of the tank allow waves to be generated in multiple directions, including monochromatic waves

and random seas. This study, however, is undertaken in current only and nominally flat water without actuation of the wave paddles. Current can also be generated in any direction. The flow is recirculated through turning vanes under the wave paddles through a chamber under the main test volume. The lower chamber is equipped with 28 propellers around the perimeter. By controlling individually the velocity of each propeller, it is possible to generate currents in excess of 1.6 m s^{-1} in any direction. The specific current conditions during the test are presented in Sect. 2.3.

2.2 Turbine

Figure 2 shows an underwater picture of the axial in-stream turbine. The diameter of the rotor is $D = 1.2$ m, and the diameter of the hemispherical hub is $0.1D$. The rotor axis is at 1 m from the floor, i.e. vertically centred with respect to still water depth. The nacelle is a torpedo $0.86D$ long, including the hub and the downstream hemispherical cap. It extends beyond the tower with a larger diameter of $0.13D$. The axis of the cylindrical tower is $0.4D$ downstream of the rotor plane and has a diameter of $0.085D$. The turbine aims to represent a realistic megawatt rated turbine at a 1:15 scale. More details on its design can be found in Payne et al. (2017).

The turbine is equipped with three blades, whose geometry is available at https://datashare.is.ed.ac.uk/handle/10283/2356. The blade pitch was kept constant at the design value.

The angular velocity of the turbine is controlled with an incremental quadrature encoder, delivering a resolution of 16,384 (14-bit) pulses per revolution. Contemporaneous angular velocity data is not available. A later repeat test of the turbine under the same ambient conditions showed a mean velocity of 88.9 Revolutions Per Minute (RPM) and a standard deviation of 1.31 RPM, equivalent to a tip speed ratio of seven.

Whilst the turbine can be equipped with sensors to measure torque, thrust, and root bending moment of each blade, these were not available at the time of the test. However, the same turbine was tested in the same flow conditions on other occasions and results from these sensors can be found in Noble et al. (2020). For a nominal inflow velocity of 0.8 m s^{-1}, Draycott et al. (2019) measured the power and thrust coefficients of this turbine as approximately 0.42 and 0.72, respectively.

2.3 Coordinate system and free stream velocity

The reference system is located on the top of the rotor disk (Fig. 2), where the x and z axes are streamwise and vertical respectively. The reference system is centred on the tip of the blade when this is vertically pointing upwards (i.e. top dead centre), within an accuracy smaller than ± 3 mm.

The free stream velocity is measured with an acoustic Doppler velocimeter (Nortek Vectrino Profiler operating in point measurement mode). This velocimeter measures three velocity components at 100 Hz with an accuracy of 1%. The current is characterised by repeating the tests in the absence of the turbine and any other underwater installation. The probe is located at 405 mm (± 1 mm) under the still water level.

The mean and root mean square of the three streamwise velocity components are presented in Table 1. The resolved turbulence intensity is calculated as 6.1%. The velocity fluctuations are similar in all axes.

Fig. 1 The 25 m diameter circular facility FloWave at the University of Edinburgh

While only a point measurement is taken, interested readers can find a description of the spatial variation of the flow field in FloWave in Noble et al. (2015). In the following, the mean streamwise velocity $U = 0.866$ m s^{-1} is used to non-dimensionalise the results.

3 Lagrangian particle tracking velocimetry

The underwater measurement system includes the LaVision LED Flashlight 300 illumination unit and the LaVision MiniShaker velocimeter. These are controlled from a Windows 10 PC using LaVision's DaVis 10 software and a programmable timing unit. The data is stored directly to the PC. Data analysis is made with the STB module in the LaVision's DaVis 10 software, which is also used for data visualisation.

3.1 Hardware

The LED Flashlight 300 unit from LaVision comprises 72 eye-safe high-powered LEDs, which are configured in an array covering an active area of 300 mm $\times$ 100 mm. The light set is enclosed in a transparent, rigid, cuboid container piercing the water. This allows the lights to shine underwater while remaining dry and accessible from above water. The container is open on the top to enhance the cooling of the LEDs, which are equipped with fans on their rear side. The lower surface of the container was not notably warmed by the LED and and thus the water convection due to the heat flux provided by the LED is probably negligible. It should be noted that this illumination configuration was constructed specifically for these initial proof-of-concept tests. An underwater LED unit was consequently developed by LaVision and it is currently available on the market.

The lights are triggered with a frequency of 256 Hz, synchronised with the MiniShaker camera module by LaVision. The LED unit is used in a pulsed-overdrive mode, with a 5% duty cycle (10% is the maximum achievable by the system), and a pulse illumination time of 190 μs.

Images are captured by a MiniShaker underwater system, which comprises four cameras. Each camera has a sensor resolution of 896 pixels $\times$ 656 pixels, that can acquire 8- or 10-bit images at a maximum of 510 frames per second, at full resolution. Here, cameras are set to record at 256 Hz at 8 bit, where the choice of 8 bit is due to a software issue that was subsequently resolved. The camera exposure time is set to 200 μs. The cameras are equipped with 7.8 mm focal length lenses. Under the current imaging conditions, the recording rate of 256 Hz was chosen such that the particle displacements in the free stream are between 10 and 11 pixels on the camera images.

Within the MiniShaker, the four cameras are placed on the same plane ($y = 600$ mm, see Fig. 2) and are pre-aligned to be used at the fixed working distance of 600 mm away from the focal plane. The two most external cameras are at a relative angle of 28°. The cameras are at a fixed position with respect to each other

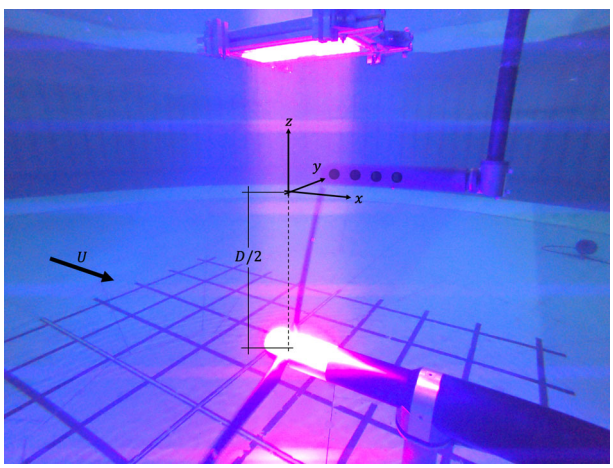

Fig. 2 Underwater picture of the tidal turbine illuminated by the LED unit placed above the hub into a container piercing the free surface, and the torpedo containing the four streamwise-aligned cameras of the MiniShaker in the background

Table 1 Flow conditions at $x = (0, 0, -0.005 \pm 0.001$ m)

Velocity component	Mean [m s^{-1}]	Root mean square [m s^{-1}]
Streamwise (x)	0.866	0.0615
Crossflow horizontal (y)	0.0139	0.0650
Vertical (z)	– 0.00715	0.0531

and, therefore, this configuration requires only a single perspective calibration to be performed at the start of the measurement campaign.

The MiniShaker camera housing is a tube of length 730 mm and diameter 100 mm (Fig. 2). This is supported by a vertical tube that guides all the cables and that has a diameter of 60 mm. The MiniShaker and the LED box are rigidly mounted to the instrumentation gantry, which allows the system to be translated for later stitching the data to give an enlarged volume of interest (VOI).

Tracer particles already present in the water from previous experimental campaigns are used. These are Potters Sphericel 110P8 glass spheres, with a diameter of ca. 12 μm and a density of 1.10 g/cc. On average, 12,000 particles are tracked in each volume, with a minimum of 10,000 particles when the blade is within the VOI. By considering an average of 12,000 particles tracked in a 896 $\times$ 656 image resolution, we estimate that the tracer particle concentration (i.e. the image source density) is around 0.02 ppp. The source density number cannot be estimated because the seeding particles used were already present in the tank (for acoustic Doppler velocimetry purposes), and no concentration measurement is performed.

3.2 Calibration

The image data from the four cameras of the MiniShaker module were acquired using the DaVis 10 platform and were subsequently analysed using the STB module of the same software platform. STB is a 4D Lagrangian particle tracking technique that identifies 3D particle positions and tracks each particle over time (Schanz et al. 2016). The starting point of the analysis is the perspective calibration of the camera system, which allows for the algorithm to reconstruct 3D particle positions by triangulating the 2D camera images. For the perspective calibration, a known target needs to be used, with markers present in at least two separate planes in the out-of-plane direction which, for the reference system in Fig. 2, is the y-direction.

In this study, a 300 mm $\times$ 300 mm calibration two-level calibration plate is imaged at three positions along y-direction, namely – 70 mm, 0 and 70 mm with respect to the mid-plane of the measurement volume. The plate has a marker diameter of 3 mm, with a dot-to-dot distance of 15 mm. The separation between the two levels of dots is 3 mm. The plate is placed such that it covers the entire camera image, and that each marker covers about 10 pixels on the calibration images.

The second step of the calibration process consists of a Volume Self-Calibration (VSC) procedure (Wieneke 2008). During this second step, the mapping function obtained during the first step is refined using particle images of tracers within the flow, as imaged by all the cameras in the system at the same instance in time. VSC is applied iteratively to approximately 500 images, by dividing the VOI in $5 \times 5 \times 3$ sub-volumes corresponding to a total physical domain of 334 mm $\times$ 244 mm $\times$ 140 mm. The total average disparity obtained after the VSC process is lower than 0.1 voxel, corresponding to a valid calibration for volumetric flow measurements (Elsinga et al. 2006).

Finally, the last step in the calibration process is the calculation of an Optical Transfer Function (OTF) (Schanz et al. 2013). As STB is based on diffraction-limited imaging, the particle image shape is directly influenced by the diffraction spot of the lens aperture and the position of the 3D particle relative to the focal plane. To accurately determine the particle image for a certain position in the VOI, an average particle image is calculated for each sub-volume as created in the VSC step and used as the basis for the calculation of the OTF, which is subsequently used in the STB processing.

3.3 Data processing

Before the STB analysis is undertaken, image pre-processing is performed on the raw data, using a combination of spatial filters. A local sliding minimum intensity value is first subtracted using a kernel of 7 pixels $\times$ 7 pixels, to reduce image noise. Second, a spatial image normalisation is applied using a local averaged image with filter length of 300 pixels, to reduce differences in particle image intensity distributions

across the camera images. A 3×3 Gaussian smoothing algorithm followed by a sharpening filter are also applied to the image.

During the initialisation of the STB analysis, a triangulation step using iterative particle reconstruction is initiated to determine the particle positions in the 3D space, followed by a "shaking" step where the 3D positions are adjusted in small steps (0.1 voxel) to find the best possible match with the particle projections in the different camera images (Wieneke 2013). During this step, the use of the OTF ensures that the optical properties of the experimental set-up are taken into consideration and allow for an accurate determination of the 3D particle positions. Furthermore, the use of time-resolved data allows the STB algorithm to use previous time steps (after an initialisation phase) to predict the new particle position at the current time-step and, therefore, speeding up the computation by removing part of the effort in the triangulation process. The initialisation phase consists of four time-steps, during which the triangulation using iterative particle reconstruction is performed as described above. The obtained particle tracks are used to create a second-order polynomial fit and extrapolated to the following time-step, providing a prediction of the new particle position. This new predicted position is also "shaken" to maximise the match with the projected 2D particle images on the individual camera frames.

The velocity field is binned to a regular grid, with bins of $96 \times 96 \times 96$ voxels (equivalent to cubes with a size of 32.4 mm), with an overlap of 83.3%. This resulted in a grid step size of 16 voxels in each direction, equivalent to 5.4 mm. The binning of track data on to a regular grid is performed using the 'convert-to-grid' function in DaVis 10. The function uses all tracks in the vicinity of a grid point to calculate the velocity (or acceleration) at that point. The contribution of a track to the grid node is weighted by the distance of the track from the node, using a Gaussian weighting function. The width of the Gaussian weighting function is chosen such that it has the same effective size, or the same spatial filtering effect, as a cube with the user-specified sub-volume size (in this case $96 \times 96 \times 96$ voxels). The binned velocity field is reported as the instantaneous velocity field ($\boldsymbol{u}$).

In this demonstrative study, we take 10,240 images for each of the seven VOIs. All data are available upon request from the corresponding author, but in this paper, we present data only from a subset of this dataset. Specifically, the mean velocity field ($\bar{\boldsymbol{u}}$) is computed from 2500 frames. The phase-averaged velocity field ($\langle \boldsymbol{u} \rangle$) is computed from 570 frames, corresponding to ten blade passes.

3.4 Uncertainty quantification

The uncertainty at 68% confidence level of the binned velocity field is calculated for each i-th velocity component as

$$U_{u_i} = \pm \frac{\sigma_{u_i}}{\sqrt{N}}, \tag{1}$$

where σ_{u_i} is the standard deviation of u_i (or $\bar{u_i}$ for the uncertainty of the time-averaged flow field) in the considered bin, and N is the number of vectors used at each grid node location.

Figure 3 shows the distribution U_{u_x} on the mid vertical plane ($y \approx 0$) of the measurement volume. The average of the uncertainty values on the plane is ± 0.003 m s^{-1} (or ± 0.03 voxel), which is 0.35% of the free stream velocity. The maximum uncertainty is in the vortex core, where it is approximately ± 0.017 m s^{-1}, therefore below 2% of the free stream velocity. The uncertainty of u_z is similar to that of u_x, whilst the uncertainty of u_y is around ± 0.005 m s^{-1} (or 0.05 voxels) on the whole plane, roughly 0.6% of the free stream velocity.

One of the main factors influencing the magnitude of the velocity uncertainty is the number of reconstructed particles in the measurement volume. The total number of reconstructed particles in the volume varies along the y-axis. The highest number of particles is found in the middle of the volume and it decreases by more than 20% towards the edges, i.e. towards and away from the Minishaker camera. The main cause for this behaviour is likely to be the distribution of light in the measurement volume. In fact, higher light intensity is expected in the middle of the volume compared to the edges. The variation in the number of reconstructed particles along the y-axis affects the uncertainties of the velocity components U_{u_x} and U_{u_z}. These uncertainties increase towards the edges of the measurement volume by approximately 15% compared to the mid-plane ($y = 0$).

The intersection angle of the camera optical axes, which varies along the y-axis, particularly affects the uncertainty U_{u_y}. In fact, the U_{u_y} averaged over a plane orthogonal to the y-axis is maximum for the farthest

plane of the measurement volume from the Minishaker camera, where it is up to 0.0065 m s^{-1}, or 30% higher than U_{u_y} averaged over the $y = 0$ plane.

The uncertainty is also affected by the passage of the blade through the measurement volume. The uncertainties U_{u_x} and U_{u_z} averaged over the planes that are intersected by a turbine blade reach approximately 0.004 m s^{-1}, which is around 33% higher than the average U_{u_x} and U_{u_z} on planes that are not intersected by a blade (e.g. y=0 in Fig. 3). The uncertainty of the out-of-plane component, U_{u_y}, is less affected by the blade passage. Its average over planes intersected by a blade turbine increase to approximately 0.006 m s^{-1}, which is 20% higher than the average U_{u_y} on planes not intersecting a blade.

The Dynamic Spatial Range (DSR), which is the ratio between the size of the VOI (994 voxels), and the size of the bins (96 voxels), is just over 10. It is noted that the DSR could be further improved by decreasing the bin size used in the conversion to grid step. Given the average number of tracks obtained of over 12,000 per time-step, a bin size down to 48 × 48 × 48 voxels could also be used to increase the DSR by a factor of 2. However, in the case of the near wake results, the DSR is increased to 73 through the stitching process because of the increased total volume size.

The Dynamic Velocity Range (DVR) is computed as the ratio between the maximum flow velocity (in this case, the streamwise velocity 0.94 m s^{-1}) and the uncertainty of the flow velocity along the same direction. By taking the uncertainty of u_x as the spatially-averaged value of ±0.003 m s^{-1} (0.03 voxel), the DVR is estimated as 313. In the vortex core, using the local uncertainty of ±0.017 m s^{-1}, the DVR is estimated in 55.

4 Example of application

In this section, two examples of results are presented to demonstrate this measurement technique. We will focus on the formation of tidal turbine's tip vortices, and their evolution up to one diameter downstream of the turbine.

4.1 Tip vortex formation

Figure 4 shows the formation of the tip vortex from the blade, which, at this time step, is approximately pointing upwards towards the free surface. The second tip vortex on the right hand side is a slide of the first helicoidal ring of the wake.

This figure is achieved by combining together two VOIs, shifted by 150 mm in the streamwise direction, resulting in 50% overlap. The two VOIs are recorded at different times. Hence, the measurements are synchronised by matching the instantaneous position of the vortex core in both volumes. The velocity field of the two measurements combined, $\boldsymbol{u} = (u, v, w)$, is used to compute the turbulent kinetic energy κ, which is plotted on the plane $y = 0$ in Fig. 4.

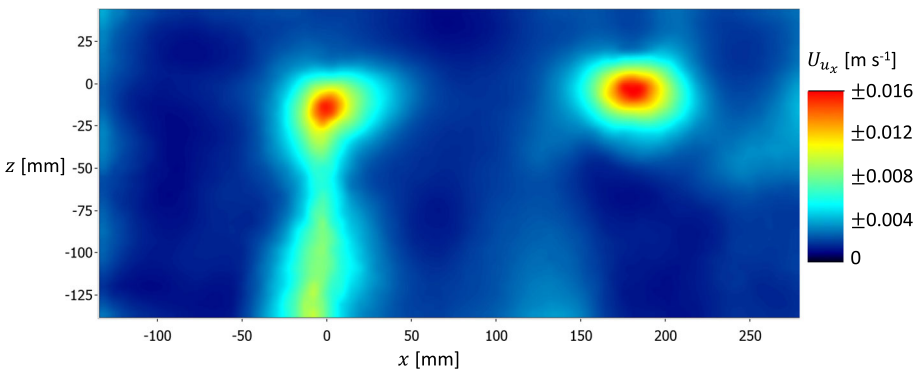

Fig. 3 Distribution of the uncertainty of the instantaneous streamwise velocity over the mid horizontal plane ($y = 0$) of the volume of interest. The coordinate system is centred at the tip of the blade, which is approx. vertical and pointing upwards. The maximum uncertainty values (in red) correspond to the core of the tip vortices

The phase-averaged velocity field $\langle \boldsymbol{u} \rangle$ is used to compute the isosurfaces of swirling strength $\langle \lambda_2 \rangle$ that identify the tip vortices in Fig. 4, and the y-component of the vorticity $\langle \omega_y \rangle$ by which the isosurfaces are coloured.

The mean streamwise convection velocity of the tip vortices is found from the phase-averaged field to be $U_v = 0.828U = 0.717$ m s^{-1}. This is taken as the streamwise velocity in the viscous core of the vortex, which is where the swirling strength is maximum. This velocity component is fairly constant, varying by less than 3% from when the vortex is formed to when it leaves the field of view. The velocity field $\langle \boldsymbol{u} \rangle - (U_v, 0, 0)$ seen by an observer travelling with the tip vortices, is illustrated by the velocity vectors on the plane $y = 0$ in Fig. 4.

These results enable new insights on the near wake behind a rotor. The role of the tip vortex on the energy entrainment from the outer flow into the wake is still a matter of debate. Lignarolo et al. (2015) argued that the tip vortices inhibit turbulent mixing of the expanding wake, in contrast to previous studies that argues that tip vortex circulation enhanced turbulent mixing (Huttter 1977).

The $\langle \boldsymbol{u} \rangle - (U_v, 0, 0)$ velocity field in Fig. 4 reveals how the velocity field is mostly governed by the induced velocity of the tip vortices. The wake expansion observed in Fig. 4, such that the tip vortex on the right hand side is higher than that being formed, is also the result of the self-induced velocity of the tip vortices. Each tip vortex experiences a positive and a negative induced vertical velocity due to the vortices downstream and upstream, respectively. The most upstream vortices have more vortices downstream than upstream, resulting in a net positive vertical velocity.

The tip vortices convect near the middle of the time-averaged shear layer, indicated by the maximum κ in Fig. 4. This figure clearly shows how each tip vortex induces a potential-like tangential velocity around their viscous core. For an observer fixed with our reference system, vortex shedding results in a periodic variation of the mean flow field, but because the flow fluctuation is periodic, it does not contribute to the production of turbulent kinetic energy. The same conclusion, i.e. that the tip vortices do not contribute to the production of turbulent kinetic energy until aperiodic instabilities occur, has been recently demonstrated by Lignarolo et al. (2015) for wind turbines using a triple decomposition of the turbulent flow fields. For this reason, closure models based on the eddy-viscosity overpredict mixing and wake recovery immediately downstream of the rotor. In fact, the eddy-viscosity model assumes that the Reynolds stress tensor is proportional to the *mean* rate of strain tensor. In unsteady Reynolds-averaged Navier-Stokes simulations, the 'mean' is typically performed over a period smaller than that of the vortex shedding. Therefore, the eddy-viscosity model incorrectly predicts higher Reynolds stresses, and thus higher production of turbulent kinetic energy.

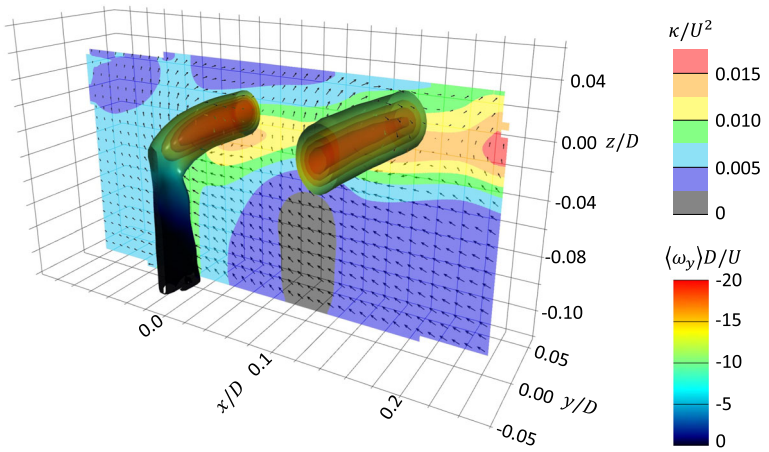

Fig. 4 Vortex generation from the tip of the blade and a slide of the tip vortex formed by the previous blade. The coordinate system is centred at the tip of the blade, which is approx. vertical and pointing upwards. Time-averaged velocity vectors of $\langle \boldsymbol{u} \rangle - (U_v, 0, 0)$, i.e. as observed from travelling downstream at the vortex convection velocity $U_v = 0.828U$ are plotted on the $y = 0$ plane (only every second vector is plotted). On this plane, we show a contour map of turbulent kinetic energy κ. Tip vortices are identified by isosurfaces, each with a fixed value of the swirling strength $\langle \lambda_2 \rangle$ of the phase-averaged flow velocity $\langle \boldsymbol{u} \rangle$. Isosurfaces are coloured by the phase-averaged y-component of the vorticity vector $\langle \omega_y \rangle$. All quantities are non-dimensionalised with the rotor diameter D and the free stream velocity U

4.2 Near wake

A further 5 VOIs are measured, by translating downstream the MiniShaker and the LED units by 200 mm steps. This gives an extended measurement volume of approximately 1400 mm $\times$ 244 mm $\times$ 140 mm.

Figure 5 shows the near wake up to $0.9D$ downstream. Similarly to Sect. 4.1, the measurements are synchronised by matching the instantaneous position of the vortex core in the overlapping regions of the VOIs. The velocity field of the seven combined VOIs includes 2500 time steps. The flow field of one of these time steps, when the blade is vertical and pointing upwards, is used to compute the isosurfaces of λ_2 and the contours of ω_y by which the isosurfaces are coloured. The isosurfaces are not as smooth as those in Fig. 4 because they are not phase-averaged. This, in fact, was not possible because a turbine encoder was not available during the experiments.

The 2500 flow fields are used also to compute the mean streamwise ($\bar{u}$) and vertical ($\bar{v}$) velocity components. Contours of the $\bar{v}/\bar{u}$ are plotted on the plane $y = 0$ in Fig. 5.

The reconstructed flow field in Fig. 5 demonstrates how this measurement technique can provide new insights on the tip vortex dynamics that lead to vortex breakdown (Okulov and Sorensen 2004; Felli et al. 2011; Posa et al. 2021). As noted by Lignarolo et al. (2015), the vortex dynamics in the near wake that precedes leapfrogging and then vortex breakdown is predicted with difficulty by low-order models, highlighting that the governing physics is not entirely understood. Furthermore, the free surface limits the wake expansion, but the resulting vortex dynamics is also not predictable by existing low order models (Adcock et al. 2021).

Here, $\bar{v}/\bar{u}$ is the arctangent of the direction of the in-plane mean velocity. Hence, by observing the contours of $\bar{v}/\bar{u}$, we can infer how the wake expands up to about $0.8D$ downstream of the turbine. This is when the vorticity of the extra vortices downstream becomes negligible and thus the net vertical induced velocity vanishes. In unconstrained flow such as, for instance, for wind turbines (Lignarolo et al. 2015) or for tidal turbines in deep water (Posa et al. 2021), the wake continues to expand well beyond one diameter downstream of the turbine. The shorter measured expansion region demonstrates the strong effect of the free surface.

The streamwise distance between the tip vortices is higher for the first four vortices. This suggests that vortex pairing begins with the 5th tip vortex at approx. $0.5D$. In contrast, vortex pairing is typically observed well after one diameter downstream of the turbine in an unconstrained stream (Sørensen 2011; Lignarolo et al. 2015). Therefore these results suggest that the free surface not only mitigates the wake expansion, but might result in earlier vortex instabilities. Future research may consider measurement volumes further downstream to confirm this hypothesis.

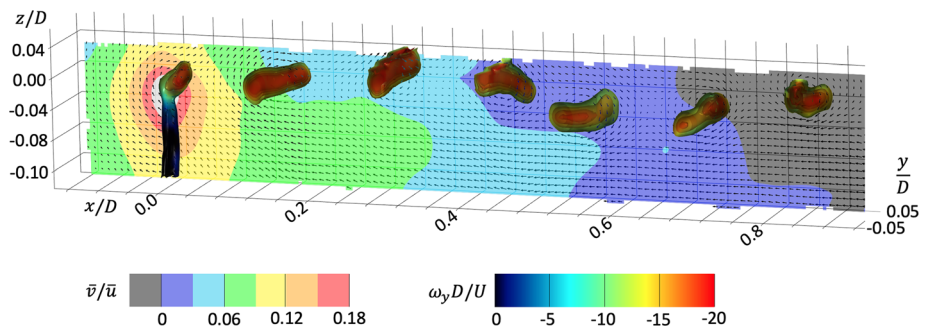

Fig. 5 A vertical slide of the tip vortices within the first turbine diameter length of the wake at the same time step and with the same reference system as in Fig. 4. Tip vortices are identified by isosurfaces, each with a fixed value of λ_2 and coloured by the local value of ω_y. Both λ_2 and ω_y are computed from the instantaneous (non phase-averaged) flow field. Time-averaged velocity vectors of $\langle \boldsymbol{u} \rangle - (U_v, 0, 0)$, i.e. as observed from travelling downstream at the vortex convection velocity $U_v = 0.828U$, are plotted on the $y = 0$ plane (only every second vector is plotted). The plane is coloured by the ratio of the vertical ($\bar{v}$) and streamwise ($\bar{u}$) time-averaged velocities. All quantities are nondimensionalised with the rotor diameter D and the free stream velocity U

5 Discussion and conclusions

This paper presents an underwater Lagrangian particle tracking velocimetry based on eye-safe LED illumination. Because this technique allows measuring relatively large volumes, it is particularly well suited for those large-scale marine facilities where laser-based techniques, such as stereo PIV, are impractical for health and safety reasons. We demonstrate this technique by measuring the near wake behind a 1:15 scale tidal turbine with a diameter of 1.2 m in a 25 m diameter, 2 m deep facility. We measure the flow field in seven volumes approximately 334 mm long, 244 mm wide and 140 mm deep. Assuming periodic flow conditions, we combine these seven volumes together with appropriate overlap to resolve the near wake within one diameter from the turbine. The flow field is measured with a temporal resolution of 3.9 ms (256 frames per seconds) and a spatial resolution of 5.4 mm.

Because the system does not need to be re-calibrated once moved, different volumes can be easily combined together. For a periodic flow such as the wake behind a rotor, this allows measurement of a phase-locked flow field. The different volumes can be easily combined if flow measurements are synchronised with a measure of the angular position of the turbine. In this example, we use the position of the vortex core in the overlap region between two adjacent volumes of interest.

Overall, the proposed methodology can enable a step change in the flow diagnostic capabilities of large scale marine facilities. The large volume and high time and spatial resolution could enable key research questions on high-Reynolds-number flows to be addressed, and could provide valuable benchmark data for numerical model development and code validation.

Acknowledgements The authors acknowledge the support from the UK Engineering and Physical Sciences Research Council (EPSRC) for funding the first author through the Grant Number EP/V009443/1. The FloWave Ocean Energy Research facility was co-funded by the EPSRC through the grant number EP/I02932X/1. The tidal turbine model was developed under the EPSRC-funded SuperGen UK Centre for Marine Energy Research (grant number EP/M014738/1). The authors are grateful to the EPSRC and the grant's Principal Investigator, Dr Aristides Kiprakis, for kindly allowing its use for this investigation.

Author Contributions IMV conceived and coordinated the study, and wrote the first draft of the manuscript. AN designed and led the experiment, with the assistance of TD and RG, and undertook the data processing. All authors edited and approved the manuscript.

Funding The study received funds from the UK Engineering and Physical Sciences Research Council (EPSRC) through the Grant Number EP/V009443/1. The study also benefited from the use of the FloWave Ocean Energy Research facility, which was funded by the UK Engineering and Physical Sciences Research Council (Grant number EP/I02932X/1) and by the use of a scale model tidal turbine, which was developed by the SuperGen UK Centre for Marine Energy Research (EP/M014738/1).

Availability of data and materials (Data Transparency) The data presented in this work are available upon request.

Declarations

Conflict of interest The second author (AN) is an employee of LaVision, which commercialises the instrumentation presented in this work. The facility FloWave, which is part of the School of Engineering of the University of Edinburgh, did not receive any external funding for this investigation.

Code availability (software application or custom code) All software used in this study is proprietary.

Ethics approval Not applicable.

Consent to participate Not applicable.

Consent for publication The data presented are owned by the authors, who all gave explicit consent to submit. The authors obtained consent to submit from The University of Edinburgh and LaVision.

References

Adcock TAA, Draper S, Willden RHJ, Vogel CR (2021) The Fluid Mechanics of Tidal Stream Energy Conversion. Annual Review of Fluid Mechanics 53:287–310

Adrian L, Adrian RJ, Westerweel J (2011) Particle image velocimetry, vol 30. Cambridge University Press, New York (**ISBN 0521440084**)

Afgan I, McNaughton J, Rolfo S, Apsley DD, Stallard T, Stansby P (2013) Turbulent flow and loading on a tidal stream turbine by LES and RANS. International Journal of Heat and Fluid Flow 43:96–108. https://doi.org/10.1016/j.ijheatfluidflow.2013.03.010

Ahmed U, Apsley DD, Afgan I, Stallard T, Stansby PK (2017) Fluctuating loads on a tidal turbine due to velocity shear and turbulence: Comparison of CFD with field data. Renewable Energy 112:235–246. https://doi.org/10.1016/j.renene.2017.05.048

Chamorro LP, Hill C, Morton S, Ellis C, Arndt REa, Sotiropoulos F (2013) On the interaction between a turbulent open channel flow and an axial-flow turbine. Journal of Fluid Mechanics 716:658–670. https://doi.org/10.1017/jfm.2012.571 (**ISBN 0022-1120**)

Chen Y, Lin B, Lin J, Wang S (2017) Experimental study of wake structure behind a horizontal axis tidal stream turbine. Applied Energy 196:82–96. https://doi.org/10.1016/j.apenergy.2017.03.126

Chételat O, Kim KC (2002) Miniature particle image velocimetry system with LED in-line illumination. Measurement Science and Technology 13(7):1006–1013. https://doi.org/10.1088/0957-0233/13/7/306

Day AH, Babarit A, Fontaine A, He Y-P, Kraskowski M, Murai M, Penesis I, Salvatore F, Shin H-K (2015) Hydrodynamic modelling of marine renewable energy devices: A state of the art review. Ocean Engineering 108:46–69. https://doi.org/10.1016/j.oceaneng.2015.05.036

Draycott S, Payne G, Steynor J, Nambiar A, Sellar B, Venugopal V (2019) An experimental investigation into non-linear wave loading on horizontal axis tidal turbines. Journal of Fluids and Structures 84:199–217. https://doi.org/10.1016/j.jfluidstructs.2018.11.004

Elsinga GE, Scarano F, Wieneke B, Van Oudheusden BW (2006) Tomographic particle image velocimetry. Experiments in Fluids 41(6):933–947. https://doi.org/10.1007/s00348-006-0212-z

Felli M, Camussi R, Di Felice F (2011) Mechanisms of evolution of the propeller wake in the transition and far fields. Journal of Fluid Mechanics 682:5–53. https://doi.org/10.1017/jfm.2011.150

Fontaine AA, Straka WA, Meyer RS, Jonson ML (2014) A 1:8.7 scale water tunnel verification & validation test of an axial flow water turbine, Technical Report SAND2014-17797R. https://www.osti.gov/servlets/purl/1171589

Gaurier B, Druault P, Ikhennicheu M, Germain G (2020) Experimental analysis of the shear flow effect on tidal turbine blade root force from three-dimensional mean flow reconstruction: Shear flow effect on tidal turbine blade. Philosophical Transactions of the Royal Society A: Mathematical, Physical and Engineering Sciences **378**(2178). https://doi.org/10.1098/rsta.2020.0001

Huttter U (1977) OPTIMUM WIND-ENERGY. Annual Review of Fluid Mechanics, 399–419

Jux C, Sciacchitano A, Schneiders JFG, Scarano F (2018) Robotic volumetric PIV of a full-scale cyclist. Exp. Fluids 59(4):1–15. https://doi.org/10.1007/s00348-018-2524-1 (**ISBN 0034801825241**)

Lignarolo LEM, Ragni D, Scarano F, Simão Ferreira CJ, Van Bussel GJW (2015) Tip-vortex instability and turbulent mixing in wind-turbine wakes. Journal of Fluid Mechanics 781:467–493. https://doi.org/10.1017/jfm.2015.470

Lloyd TP, Turnock SR, Humphrey VF (2014) Assessing the influence of inflow turbulence on noise and performance of a tidal turbine using large eddy simulations. Renewable Energy 71:742–754. https://doi.org/10.1016/j.renene.2014.06.011 (**ISBN 0960-1481**)

Lust E, Luznik L, Flack K, Barros J (2015) Near Wake Flow Field Measurements of a Marine Current Turbine: Preliminary Results. Oceans 2015:3–8

Mertens C, Sciacchitano A, van Oudheusden BW, Sodja J (2021) An integrated measurement approach for the determination of the aerodynamic loads and structural motion for unsteady airfoils. J. Fluids Struct. 103:103293. https://doi.org/10.1016/j.jfluidstructs.2021.103293

Noble DR, Davey TAD, Smith HCM, Kaklis P, Robinson A, Bruce T (2015) Spatial variation in currents generated in the FloWave Ocean Energy Research Facility. Proceedings of the 11th European Wave and Tidal Energy Conference (EWTEC2015)

Noble DR, Draycott S, Nambiar A, Sellar BG, Steynor J, Kiprakis A (2020) Experimental assessment of flow, performance, and loads for tidal turbines in a closely-spaced array. Energies **13**(8). https://doi.org/10.3390/en13081977

Nuernberg M, Tao L (2018) Experimental study of wake characteristics in tidal turbine arrays. Renewable Energy 127(2018):168–181. https://doi.org/10.1016/j.renene.2018.04.053

Okulov VL, Sorensen JN (2004) Instability of a vortex wake behind wind turbines. Doklady Physics 49(12):772–777. https://doi.org/10.1134/1.1848637

Olczak A, Stallard T, Feng T, Stansby PK (2016) Comparison of a RANS blade element model for tidal turbine arrays with laboratory scale measurements of wake velocity and rotor thrust. Journal of Fluids and Structures 64:87–106. https://doi.org/10.1016/j.jfluidstructs.2016.04.001

Ouro P, Stoesser T (2019) Impact of Environmental Turbulence on the Performance and Loadings of a Tidal Stream Turbine. Flow, Turbulence and Combustion 102(3):613–639. https://doi.org/10.1007/s10494-018-9975-6

Payne GS, Stallard T, Martinez R (2017) Design and manufacture of a bed supported tidal turbine model for blade and shaft load measurement in turbulent flow and waves. Renewable Energy 107:312–326. https://doi.org/10.1016/j.renene.2017.01.068

Posa A, Broglia R, Balaras E (2021) Instability of the tip vortices shed by an axial-flow turbine in uniform flow. Journal of Fluid Mechanics 920:1–35. https://doi.org/10.1017/jfm.2021.433

Raffel M, Willert CE, Wereley ST, Kompenhaus J, Scarano F, Kähler CJ, Wereley ST, Kompenhaus J (2018) Particle image velocimetry: A practical guide, 3rd edn. Springer, Berlin, Heidelberg

Roettig F, Wennemar K, Hoyer K, Beslac R, Hesseling C, Beck T, Friedhoff B (2019) Volumetric Flow Measurements in the Wake of a Ducted Propeller, in Proceedings of the Sixth International Conference on Advanced Model Measurement Technology for The Maritime Industry, Rome, Italy, pp. 1–14

Schanz D, Gesemann S, Schröder A (2016) Shake-The-Box: Lagrangian particle tracking at high particle image densities. Experiments in Fluids 57(5):1–27. https://doi.org/10.1007/s00348-016-2157-1

Schanz D, Huhn F, Schröder A (2018) Large-Scale Volumetric Flow Measurement of a Thermal Plume Using Lagrangian Particle Tracking (Shake-The-Box), in Particle Image Velocimetry — A Practical Guide, ed. by M. Raffel, C.E. Willert, F. Scarano, C.J. Kähler, S.T. Wereley, J. Kompenhans (Springer, Berlin, Heidelberg), pp. 606–610. Chap. 18

Schanz D, Gesemann S, Schröder A, Wieneke B, Novara M (2013) Non-uniform optical transfer functions in particle imaging: Calibration and application to tomographic reconstruction. Measurement Science and Technology **24**(2). https://doi.org/10.1088/0957-0233/24/2/024009

Schneiders JFG, Scarano F, Jux C, Sciacchitano A (2018) Coaxial volumetric velocimetry. Meas. Sci. Technol. **29**(6). https://doi.org/10.1088/1361-6501/aab07d

Shi W, Atlar M, Norman R (2017) Detailed flow measurement of the field around tidal turbines with and without biomimetic leading-edge tubercles. Renewable Energy 111:688–707. https://doi.org/10.1016/j.renene.2017.04.053

Sørensen JN (2011) Aerodynamic Aspects of Wind Energy Conversion. Annual Review of Fluid Mechanics 43, 427–448. ISBN 0066-4189\n978-0-8243-0743-1. https://doi.org/10.1146/annurev-fluid-122109-160801

Stallard T, Feng T, Stansby PK (2015) Experimental study of the mean wake of a tidal stream rotor in a shallow turbulent flow. Journal of Fluids and Structures 54:235–246. https://doi.org/10.1016/j.jfluidstructs.2014.10.017

Stallard T, Collings R, Feng T, Whelan J (2013) Interactions betweem tidal turbine wakes: Experimental study of a group of 3-bladed rotors. Philosophical Transactions of the Royal Society of London: A 371(1985):1471–2962

Tedds SC, Owen I, Poole RJ (2014) Near-wake characteristics of a model horizontal axis tidal stream turbine. Renewable Energy 63:222–235. ISBN 0960-1481 https://doi.org/10.1016 j.renene.2013.09.011

Usherwood JR, Cheney JA, Song J, Windsor SP, Stevenson JPJ, Dierksheide U, Nila A, Bomphrey RJ (2020) High aerodynamic lift from the tail reduces drag in gliding raptors. Journal of Experimental Biology **223**(3). https://doi.org/10.1242/jeb.214809

Wieneke B (2008) Volume self-calibration for 3D particle image velocimetry. Experiments in Fluids 45(4):549–556. https://doi.org/10.1007/s00348-008-0521-5

Wieneke B (2013) Iterative reconstruction of volumetric particle distribution. Measurement Science and Technology **24**(2). https://doi.org/10.1088/0957-0233/24/2/024008

Willert C, Stasicki B, Klinner J, Moessner S (2010) Pulsed operation of high-power light emitting diodes for imaging flow velocimetry. Measurement Science and Technology **21**(7). https://doi.org/10.1088/0957-0233/21/7/075402